Acta Pharmaceutica Sinica B 2025;15(10):5277−5293

Chinese Pharmaceutical Association
Institute of Materia Medica, Chinese Academy of Medical Sciences

Acta Pharmaceutica Sinica B

www.elsevier.com/locate/apsb
www.sciencedirect.com

ORIGINAL ARTICLE

Natural killer cell-derived granzyme B as a therapeutic target for alleviating graft injury during liver transplantation

Kai Wang[a,†], Zhoucheng Wang[b,†], Xin Shao[c,d,†], Lijun Meng[e,†], Chuanjun Liu[f], Nasha Qiu[e,g], Wenwen Ge[b], Yutong Chen[g], Xiao Tang[b], Xiaodong Wang[g], Zhengxing Lian[e], Ruhong Zhou[h,i], Shusen Zheng[j,k], Xiaohui Fan[c,d,*], Xiao Xu[a,k,*]

[a]*General Surgery, Cancer Center, Department of Hepatobiliary & Pancreatic Surgery and Minimally Invasive Surgery, Zhejiang Provincial People's Hospital (Affiliated People's Hospital), Hangzhou Medical College, Hangzhou 310024, China*
[b]*Department of Surgery, Zhejiang University School of Medicine, Hangzhou 310058, China*
[c]*Pharmaceutical Informatics Institute, College of Pharmaceutical Sciences, Zhejiang University, Hangzhou 310058, China*
[d]*National Key Laboratory of Chinese Medicine Modernization, Innovation Center of Yangtze River Delta, Zhejiang University, Jiaxing 314103, China*
[e]*Key Laboratory of Integrated Oncology and Intelligent Medicine of Zhejiang Province, Affiliated Hangzhou First People's Hospital, School of Medicine, Westlake University, Hangzhou 310006, China*
[f]*College of Life Sciences, University of Chinese Academy of Sciences, Beijing 100049, China*
[g]*The Fourth School of Clinical Medicine, Zhejiang Chinese Medical University, Hangzhou 310053, China*
[h]*Institute of Quantitative Biology, Shanghai Institute for Advanced Study, College of Life Sciences, Zhejiang University, Hangzhou 310027, China*
[i]*Department of Chemistry, Columbia University, New York, NY 10027, USA*
[j]*Shulan Hospital Affiliated to Zhejiang Shuren University, Shulan International Medical College, Hangzhou 310015, China*
[k]*NHC Key Laboratory of Combined Multi-organ Transplantation, Hangzhou 310003, China*

Received 16 September 2024; received in revised form 29 December 2024; accepted 12 March 2025

*Corresponding authors.
E-mail addresses: fanxh@zju.edu.cn (Xiaohui Fan), zjxu@zju.edu.cn (Xiao Xu).
[†]These authors made equal contributions to this work.
Peer review under the responsibility of Chinese Pharmaceutical Association and Institute of Materia Medica, Chinese Academy of Medical Sciences.

https://doi.org/10.1016/j.apsb.2025.07.042

KEY WORDS

Natural killer cells;
Granzyme B;
Hepatic ischemia-reperfusion injury;
Liver transplantation;
Nanomedicine;
Adoptive immunotherapy;
Molecular dynamics;
Translational medicine

Abstract Liver transplantation (LT) has become a standard treatment for end-stage liver diseases, and graft injury is intricately associated with poor prognosis. Granzyme B (GZMB) plays a vital role in natural killer (NK) cell biology, but whether NK-derived GZMB affects graft injury remains elusive. Through the analysis of single-cell RNA-sequencing data obtained from human LT grafts and the isolation of lymphocytes from mouse livers following ischemia-reperfusion injury (IRI), we demonstrated that 2NK cells with high expression of GZMB are enriched in patients and mice. Both systemically and liver-targeted depletion of NK cells led to a notable reduction in $GZMB^+$ cell infiltration, subsequently resulting in diminished graft injury. Notably, the reconstitution of *Il2rg*$^{-/-}$*Rag2*$^{-/-}$ mice with purified *Gzmb*-KO NK cells demonstrated superior outcomes compared to those with wild-type NK cells. Crucially, global knockout of GZMB and pharmacological inhibition exhibited remarkable improvements in liver function in both mouse IRI and rat LT models. Moreover, a phosphorylated derivative of FDA-approved vidarabine was identified as an effective inhibitor of mouse GZMB activity by molecular dynamics, which could provide a potential avenue for therapeutic intervention. Therefore, targeting NK cell-derived GZMB during the LT process suggests potential therapeutic strategies to improve post-transplant outcomes.

1. Introduction

Liver transplantation (LT) has become a standard treatment for end-stage liver diseases[1]. Liver graft ischemia reperfusion injury (IRI) is a common physiopathological process during LT and is a major cause of early allograft dysfunction (EAD) and primary non-function (PNF), leading to severe complications or even mortality[2,3]. Finding ways to mitigate IRI is crucial for improving post-transplant outcomes[4]. Despite its clinical importance, the mechanisms underlying IRI are only partially understood, and effective preventive and therapeutic strategies are urgently needed[5,6].

During IRI, known as a sterile inflammation, the host's innate immunity is activated, converting the liver from an immunologically quiescent state to an inflamed organ[7]. NK cells primarily contribute to the innate immunity and represent one of the most abundant populations in the human liver[8]. NK cells play a critical role in anti-viral[9] and anti-tumor responses[10], but their role in hepatic IRI remains unclear[11]. Beldi et al.[12] reported that CD39-mediated NK cell activation enhanced IFN-γ production and contributed to hepatic IRI. However, it has also been reported that NK cell depletion may not affect liver function after IRI, which is demonstrated by unchanged liver function assays and infiltrated myeloperoxidase content[13].

Upon activation, NK cells can exert cytotoxic effects by releasing perforin, granzymes, and pro-inflammatory compounds such as IFN-γ and TNF-α, providing early defense against virus-infected or tumor cells[14]. GZMB is the most abundant one, causing apoptosis by various pathways, including cleaving and activating several proapoptotic proteins in response to infection by the perforin-dependent cytotoxic response pathway[15]. It has been previously identified as a major toxic protein in ischemic diseases such as stroke and myocardial infarction[16,17]. Santos-Zas et al.[17] found that GZMB deficiency reduced apoptosis and pro-inflammatory cytokine expression, and limited post-ischemic cardiac damage. However, NK cell-derived GZMB has not been reported or interfered with as a therapeutic target in hepatic IRI.

In this study, single-cell transcriptomics has pinpointed $GZMB^+$ NK cells as notably prevalent infiltrates in post-transplant human livers. Additionally, serum GZMB levels in recipients positively correlate with serum total bilirubin and aspartate aminotransferase following LT. Reconstitution of *Il2rg*$^{-/-}$*Rag2*$^{-/-}$ mice with purified *Gzmb*-KO NK cells resulted in less detrimental effects compared to those adoptively transferred with wild-type NK cells. Both systemic and liver-specific NK cell depletion, alongside genetic or pharmacological inhibition of GZMB, have demonstrated protective effects against liver graft injury in mouse or rat models. A phosphorylated derivative of US Food and Drug Administration (FDA)-approved vidarabine (vidarabine phosphate) effectively suppressed GZMB activity in murine livers and reduced hepatic IRI, which could potentially be applied in clinical settings.

2. Materials and methods

2.1. Human liver tissues and serum

Liver and serum samples were obtained from individuals who underwent orthotopic LT at Shulan Hospital (Hangzhou). Liver tissues of each graft were collected at two different time points: during static cold storage (pre-LT) and 2 h after portal reperfusion (post-LT). Peripheral blood samples were collected 2 h after portal reperfusion, and serum was separated for further examination. Written informed consent was obtained from all patients. This research was approved by the Institutional Review Board of Shulan Hospital of Hangzhou (KY2023029) and complied with the ethical principles of the 1975 Helsinki Declaration.

2.2. Processing of scRNA-seq datasets

Three cohorts of human LT data were obtained from GSE171539, GSE189539, and HRA003896. The raw data was processed using Seurat, with gene symbols being revised according to the National Center for Biotechnology Information gene data (https://www.ncbi.nlm.nih.gov/gene/). Unmatched genes and duplicate genes were manually removed. The Harmony algorithm incorporated donor, platform as two technical covariates for correction purposes, assigning corresponding theta values to 4 and 2,

respectively. Principal component analysis (PCA) was then conducted, followed by uniform manifold approximation and projection (UMAP) analysis for dimensional reduction and clustering analysis. For the second round of clustering, the clusters of NK cells were extracted and integrated using canonical correlation analysis (CCA) in Seurat. NK cells were filtered using known markers in CellMatch and re-clustered to identify $GZMB^+$ NK cells based on the gene expression of *GZMB*.

2.3. Animals

Male C57BL/6 mice and Sprague−Dawley (SD) rats were housed in a controlled pathogen-free environment with a regulated temperature of 23 ± 2 °C and a 12-h light/dark cycle. The mice used in the experiment were aged around 8 weeks with an average weight of 23 ± 2 g, while the rats were aged around 7 weeks with an average weight of 250 ± 10 g. All animal procedures were approved by the Institutional Review Board of the Institutional Animal Care and Use Committee, Zhejiang Center of Laboratory Animals (Approval No. ZJCLA-IACUC-20010232), and were performed in accordance with the Guide for the Care and Use of Laboratory Animals.

Gzmb-KO mice and *Il2rg*$^{-/-}$*Rag2*$^{-/-}$ (B6RG) mice were obtained from Cyagen Biosciences (Shanghai, China). The identification primer sequences for *Gzmb*-KO mice were F: 5′-CCTTGTCCATCACTCTTCCATTGT-3′; R: 5′-TCAAACATACTTATGACTTCCCT-3′. Wild type (WT) mouse identification primer sequences were F: 5′-CCTTGTCCATCACTCTTCCATTGT-3′; R: 5′-AAAGGAAGGTGTTGCTTACTCACC-3′. All the animals were kept under standardized conditions with free access to clean water and normal chow. Genomic DNA was extracted from the tail tissue of newborn mice for genotyping by polymerase chain reaction (PCR). The representative genotyping image is shown in Supporting Information Fig. S1.

2.4. Murine hepatic IRI model

Mouse hepatic IRI was performed by 90 min of vascular occlusion of the left and mid-hepatic lobes and followed by 6 h of blood reperfusion, while the Sham group mice only performed laparotomy and abdominal closure. Animals were placed on a warm pad maintained at 37 °C until completely awake. After surgery, all mice were humanely sacrificed, and both serum and liver tissue samples were collected for further analysis.

To assess the involvement of NK cells in hepatic IRI, C57BL/6 mice received peritoneal injections of *in vivo* MAb anti-mouse NK1.1 (αNK1.1) (BioXcell, Lebanon, USA) (100 μg diluted in 200 μL dilution buffer per mouse) or *in vivo* Pure pH 7.0 Dilution Buffer (BioXcell, Lebanon, USA) (200 μL/mouse/time) three times a week prior to surgery. For liver-targeted NK cell depletion, αNK1.1 was intravenously injected at half the dosage (50 μg packed in nanoparticles per mouse) three times a week prior to surgery, while the control mice were injected with the same volume of PBS.

To evaluate the role of GZMB in hepatic IRI, both WT and *Gzmb*-KO mice underwent the same procedures. For serine protease inhibitor AEBSF (Selleck, Houston, USA), mice received peritoneal injections at a single dose of 80 mg/kg 1 h before hepatic IRI. For Vidarabine phosphate (TargetMol Chemicals Inc., Boston, USA), mice received peritoneal injections at a single dose of 100 mg/kg 12 h before hepatic IRI, and Cytarabine (Selleck, Houston, USA) was applied in another group of mice at the same dose to avoid interference from the antiviral drug's effects.

2.5. Rat LT model

Rat orthotopic LT was conducted in accordance with previously described methodologies at our esteemed institution[18]. Prior to the LT procedure, the rats underwent an overnight period of fasting. To induce sufficient cold ischemia, all liver grafts were subjected to cold storage in a solution of normal saline before subsequent revascularization. The experimental rats were divided into three distinct groups: (1) Sham Group ($n = 6$); (2) LT+PBS Group: peritoneal injection of 20 mL/kg PBS 6 h before transplantation ($n = 6$); (3) LT+AEBSF Group: peritoneal injection of 20 mL/kg mL PBS containing 60 mg/kg AEBSF ($n = 6$). Twenty-four hours after transplantation, rats were humanely sacrificed, and both serum and liver tissue samples were collected for further analysis.

2.6. NK cell purification and adoptive transfer

NK cells were extracted from WT or *Gzmb*-KO C57BL/6 mice spleens, and subsequently purified using an NK Cell Isolation Kit, mouse (Miltenyi Biotec, Bergisch Gladbach, Germany) according to the manufacturer's protocol. Briefly, 8-week-old *Gzmb*-KO or WT C57BL/6 mice were humanely euthanized to isolate splenocytes, and then NK cells were negatively selected using a combination of antibody-coated magnetic beads (CD3, CD4, CD8, CD19, Anti-MHC-class II, F4/80, Ly-6G, and TER-119) to remove non-NK cells, thus yielding NK cells with a purity exceeding 90%.

To demonstrate the specific role of NK-derived GZMB in mediating hepatocyte cytotoxicity, NK cells from *Gzmb*-KO or WT C57BL/6 mice were adoptively transferred into *Il2rg*$^{-/-}$*Rag2*$^{-/-}$ mice according to previously published protocols[19]. A total of 1×10^6 NK cells suspended in 200 μL sterile PBS were intravenously administered into *Il2rg*$^{-/-}$*Rag2*$^{-/-}$ mice, while the other were intravenously injected with 200 μL PBS only. The transferred NK cells were allowed to undergo *in vivo* expansion for 5 days, then all the mice underwent hepatic IRI as described above.

2.7. Cell culture and recombinant mouse GZMB protein treatment

Alpha mouse liver 12 (AML-12) cells (normal mouse hepatocytes) were cultured at 37 °C in a humidified atmosphere with 5% CO_2 in DMEM/F12 medium (Merck, Darmstadt, Germany) supplemented with 10% heat-inactivated Fetal Bovine Serum (BioChannel, Nanjing, China), 1% Penicillin−Streptomycin (Biosharp, Hefei, China), 1% Insulin-Transferrin-Selenium-Sodium Pyruvate (ITS-A) (Procell, Wuhan, China), and 40 ng/mL Dexamethasone (MedChemExpress, NJ, USA).

In order to imitate the process of HIRI *in vitro*, AML-12 cells were changed to non-serum culture media and incubated under hypoxic conditions (37 °C, 5% CO_2, and 1% O_2) for 24 h, and then changed to a normal cell incubator with oxygenation for another 12 h. In order to evaluate the effect of GZMB on hepatocyte apoptosis, recombinant mouse GZMB protein (MedChemExpress, NJ, USA) was added to the medium during reoxygenation to simulate the GZMB released by NK cells during portal reperfusion in liver transplantation. Cells were harvested for

total protein and RNA extraction and then further analysed by Western blot and RNA-seq.

2.8. Flow cytometry

Liver-infiltrated immune cells were obtained from mice using collagenase II/IV (Gibco, Grand Island, USA) and Mouse Lymphocyte Separation Medium (Dakewe Biotech, Shenzhen, China). To conduct cytometric analysis, a brief procedure was followed. Initially, the nonspecific binding of cells was blocked using purified Rat Anti-Mouse CD16/CD32 (Mouse BD Fc Block) (BD Bioscience, Franklin Lakes, USA). Following a 10-min incubation at 4 °C, cells were then stained with surface antigen−antibodies (BD Bioscience, Franklin Lakes, USA) against Fixable Viability Stain 780, PE Rat Anti-Mouse CD45, FITC Hamster Anti-Mouse CD3e, APC Mouse Anti-Mouse NK-1.1 for 30 min at 4 °C. Cells were then fixed and permeablized withFixation/Permeabilization Kit (BD Bioscience, Franklin Lakes, USA) following instructions, and stained with intracellular PE-Cyanine7 Granzyme B Monoclonal Antibody (Invitrogen, CA, USA) for 30 min at 4 °C. After washed twice with PBS, cells were analyzed using a BD CantoII flow cytometer (BD Bioscience, Franklin Lakes, USA). The obtained data were analyzed using FlowJo software (Version 10.8.1).

2.9. Nanoparticle delivery system

Herein, we developed a liver-targeted lipid nanoparticle system that effectively delivers αNK1.1[20,21]. Generally, a thin lipid film was obtained by dissolving neutral-charged helper lipids DOPC (Avanti, AL, USA) and cationic lipid DOTAP (Avanti, AL, USA) at a molar ratio of 3:1 in chloroform, followed by the evaporation of the solvent. The HEPES buffer (pH = 7.4) was then supplemented and gently stirred for 3 h at room temperature, followed by 10 min of sonication. Subsequently, the αNK1.1 solution (4.69 mg/mL) was added dropwise to the lipid solution and stirred for another 2 h at room temperature. Finally, DSPE-PEG-Gal was added to the above mixture and stirred for 15 min to obtain G-LNP/αNK1.1 at 50 °C. Consequently, the sizes and zeta potentials of the G-LNP/αNK1.1 were measured by Zetasizer Nano-ZS (Malvern Instruments, Malvern, UK) at 25 °C, and the optimized concentration of αNK1.1 was 125 μg/mL. For the treatment study, mice were i.v. administered with G-LNP/αNK1.1 three times a week prior to surgery, while the control mice were injected with an equal volume of PBS.

2.10. Surface plasmon resonance (SPR) assays

The forementioned recombinant mouse GZMB protein, AEBSF, and Vidarabine phosphate were separately diluted in sodium acetate to a concentration of 50 μg/mL. Then, the protein was immobilized on a CM5 sensor chip (Cytiva, #BR100530) using the amine coupling kit (Cytiva, #BR100050) to a final concentration of about 10,000 response units (RU)/flow cell. SPR measurements were performed at 25 °C using a Biacore (Cytiva, 8K) instrument. To determine the binding affinities, increasing concentrations of small molecules were injected onto the surface of the chip for 150 s at a flow rate of 30 μL/min, followed by a dissociation period of 300 s. Experimental data were collected and analyzed using Biacore Insight Evaluation software (Cytiva, Marlborough, MA, USA). The kinetic constant of binding was calculated using a 1:1 Langmuir affinity model.

2.11. Theoretical modelling and molecular dynamics (MD) simulations

In the absence of an experimentally determined crystal structure for mouse GZMB, AlphaFold2 was adopted to generate the protein 3D structure[22]. Subsequently, the model underwent molecular dynamics (MD) simulations for equilibration purposes. Small molecular ligands were then computationally aligned within the catalytic site of the stabilized enzyme *via* AutoDock Vina[23]. Further MD simulations were conducted to scrutinize the stability and behavior of the resultant complexes.

The MD simulation frameworks were meticulously assembled and executed utilizing the GROMACS suite[24], with the resulting trajectories subjected to rigorous analysis through the Visual Molecular Dynamics (VMD) software[25]. The protein or complex was solvated with a 150 mmol/L NaCl electrolyte. We applied the CHARMM36 force field[26] for protein and ions, the TIP3P model for water molecules. The force fields of small molecules were generated using CGenFF[27]. Simulations proceeded with a temporal resolution of 2 fs. van der Waals interactions were smoothed out between 0.10 and 0.12 nm, while long-range electrostatic forces were calculated employing the particle-mesh Ewald technique with a grid spacing of 0.1 nm. The production simulations were performed within the NPT ensemble, maintaining pressure at 1 bar *via* the isotropic Parrinello−Rahman barostat and temperature at 310 K through the Nose−Hoover thermostats.

2.12. Liver biochemical measurement

The levels of alanine aminotransferase (ALT), aspartate aminotransferase (AST), and total bilirubin (TBIL) in the serum or plasma were assessed utilizing an automated biochemical analyzer (Rayto, Shenzhen, China) in accordance with the provided guidelines.

To ascertain the concentration of GZMB, both human and mouse serum or plasma samples were employed, and the analysis was conducted utilizing commercial enzyme-linked immunosorbent assay (ELISA) kits (Cloud-Clone Corp., Houston, TX, USA) as per the manufacturer's instructions.

2.13. Histopathological and immunofluorescence analyses

The liver tissues were fixed with 4% paraformaldehyde fixing solution, dried, immersed in paraffin, and divided (5 μm thick) to determine the degree of liver necrosis. Consequently, hematoxylin and eosin (H&E) were employed to stain the sections to assess the degree of liver necrosis. Immunohistochemistry (IHC) was utilized to assess GZMB (abcam, Cambridge, UK), NK1.1 (CD161) (abcam, Cambridge, UK), and cleaved caspase 3 (C-CAS3, ServiceBio, Wuhan, China). All sections were scanned by Research Slide Scanner (Olympus, SLIDEVIEW VS200) under bright field. Necrotic areas in random fields on each HE slide were characterized by architecture loss, vacuolization, increased karyolysis, and eosinophilia. Two expert pathologists independently assessed the histological criteria for liver damage using the Suzuki score (congestion, vacuolization, and necrosis), as previously described[28]. The percentage of positive areas in the representative view of IHC slides was calculated with ImageJ software (Version 1.8.0_172).

Liver sections for immunofluorescence (IF) analysis were permeabilized using 0.2% Triton X-100 in PBS for 30 min at room temperature, then blocked with 3% BSA for 30 min at room

temperature, and incubated with primary antibodies against CD56, GZMB, and NK1.1 (CD161) (abcam, Cambridge, UK). Sections were washed with PBS and incubated with a mixture of appropriate secondary antibodies for 1 h at room temperature, 4′,6-diamidino-2-phenylindole (DAPI) was used to counterstain cell nuclei. To evaluate cell apoptosis in the liver tissue slides, terminal deoxynucleotidyl transferase dUTP nick end labeling (TUNEL) staining (ServiceBio, Wuhan, China) was performed according to the manufacturer's instructions and a previous report[29]. The digital images of immunofluorescence were acquired with fluorescence microscopy (Olympus, BX63). The percentage of positive areas in the representative view of IF slides was calculated with ImageJ software (Version 1.8.0_172).

2.14. Quantitative real-time PCR

Total RNA from cells or liver tissues was extracted using MolPure RNA Kit (Yeasen, Shanghai, China) according to the manufacturer's instructions and measured using a Nanodrop (ThermoFisher, MA, USA). Reverse transcription of RNA was performed on S1000 Thermal Cycler (Bio-Rad, Hercules, USA) by using Hifair V one-step RT-gDNA digestion SuperMix (Yeasen, Shanghai, China). Quantitative real-time PCR was performed on a Light Cycler 480 (Roche, Basel, Switzerland) with Hieff SYBR Green Master Mix (Yeasen, Shanghai, China). The primers used were synthesized by Tsingke Biotech (Beijing, China) and listed in Supporting Information Table S1.

2.15. Western blot analysis

Total proteins from liver tissues were extracted using RIPA lysis buffer supplemented with protease inhibitor, protein phosphorylase inhibitors, and PMSF (Fdbio, Hangzhou, China). The protein concentration in the lysates was determined using a BCA protein assay (Beyotime, Shanghai, China). Subsequently, the protein supernatants were mixed with 5 × SDS loading buffer and denatured at 95 °C for 10 min. Protein samples were separated by 4%−20% sodium dodecyl sulfate polyacrylamide gel electrophoresis and then transferred onto polyvinylidene fluoride (PVDF) membranes (Millipore, Billerica, MA, USA). The PVDF membranes were blocked with 5% BSA for 1 h at room temperature and incubated overnight at 4 °C with specific primary antibodies against BAX (CST, MA, USA), BCL2 (abcam, Cambridge, UK), C-CAS3 (CST, MA, USA), β-actin (ABclonal, Wuhan, China). Following this, the membranes were washed with TBST and incubated with an HRP-conjugated secondary antibody (anti-rabbit or anti-mouse) for 1 h at room temperature. Visualization was achieved using ECL detection kits (Fdbio, Hangzhou, China). The images were captured using the ChemiDoc Touch Imaging System (Bio-Rad, Hercules, CA, USA) and quantified using ImageJ software (Version 1.8.0_172).

2.16. Statistical analysis

All data are presented as mean ± standard error of mean (SEM). The unpaired two-tailed Student's *t*-test was employed to analyze normally distributed data between two groups, while one-way analysis of variance (ANOVA) was used to compare data among multiple groups. All statistical analyses were performed using GraphPad Prism Software (Version 8.0.1). The levels of significance are denoted as follows: $*P < 0.05$, $**P < 0.01$, $***P < 0.001$, $****P < 0.0001$.

3. Results

3.1. Single-cell RNA-seq data revealed a significant increase in $GZMB^+$ NK cells in human transplanted livers after reperfusion

To elucidate the specific infiltration pattern of NK cells in post-transplant livers, three single-cell RNA-seq datasets of human LT during the condition of cold preservation (CP) and portal reperfusion (PR) were accessed from our previous work (GSE171539 and GSE189539) and an additional dataset (HRA003896). The UMAP plots unveil a total of 114,705 cells from 20 samples, and 14 cell types have been clarified (Fig. 1A). As expected, NK cells were one of the main cell components in liver grafts before and after transplantation (Fig. 1B and C). The expression of *GZMB* and the distribution of $GZMB^+$ NK cells among the total NK cell population were acquired from the CP and PR groups, respectively (Fig. 1D). Both the percentage of $GZMB^+$ NK cells among total NK cells and the expression of *GZMB* among total NK or immune cells were significantly higher in the PR group compared to the CP group, suggesting that $GZMB^+$ NK cells may play a pivotal role in mediating liver injury after transplantation (Fig. 1E and F, Supporting Information Fig. S2A). Representative images of immunofluorescence co-staining of NK cells and GZMB in transplanted livers after portal reperfusion are depicted in Fig. 1G. It is known that T cells may also upregulate their GZMB in order to exert a cell-killing effect; however, the expression of *GZMB* was significantly lower in T cells than that in NK cells (Fig. S2B and S2C). These findings demonstrated a significant increase in $GZMB^+$ NK cells in human transplanted livers following portal reperfusion during clinical LT, which may play a critical role in inducing graft injury and affect post-transplant prognosis.

3.2. NK cells with high expression of GZMB were enriched in recipients after LT

In human liver biopsies obtained from recipients, we observed the infiltration of NK cells and the diffusion of GZMB in the ischemic liver tissue after 2 h of portal perfusion (Fig. 1G). Notably, $GZMB^+$ cells exhibited a predominant colocalization with NK cells, as revealed by multiple immunofluorescence staining. Furthermore, we investigated the genetic expression of *GZMB* in 31 pairs of human livers and the relationship between circulating GZMB levels and clinical outcomes in 35 recipients at our center (Supporting Information Table S2). Liver tissue samples were obtained on the back table (pre-LT) and 2 h after reperfusion of the transplanted liver (post-LT), while peripheral blood samples were collected right before abdominal closure. The intrahepatic expression of the *GZMB* gene was significantly increased after transplantation (Fig. 1H). Interestingly, recipients with higher circulating levels of GZMB were at a higher risk of experiencing severe liver injury, as evidenced by elevated levels of serum TBIL ($R^2 = 0.5604$, $P < 0.0001$) and AST ($R^2 = 0.2674$, $P = 0.0015$) on the third day after LT (Fig. 1I and Supporting Information Table S3). However, no significant correlation was observed between GZMB and ALT ($R^2 = 0.09905$, $P = 0.0656$).

3.3. GZMB-expressing NK cells were recruited in the ischemic liver tissue in the murine hepatic IRI model

Next, we employed an experimental model of hepatic IRI in C57BL/6 mice. Following the surgery, cell suspensions of digested livers were subjected to flow cytometry analysis. NK cells

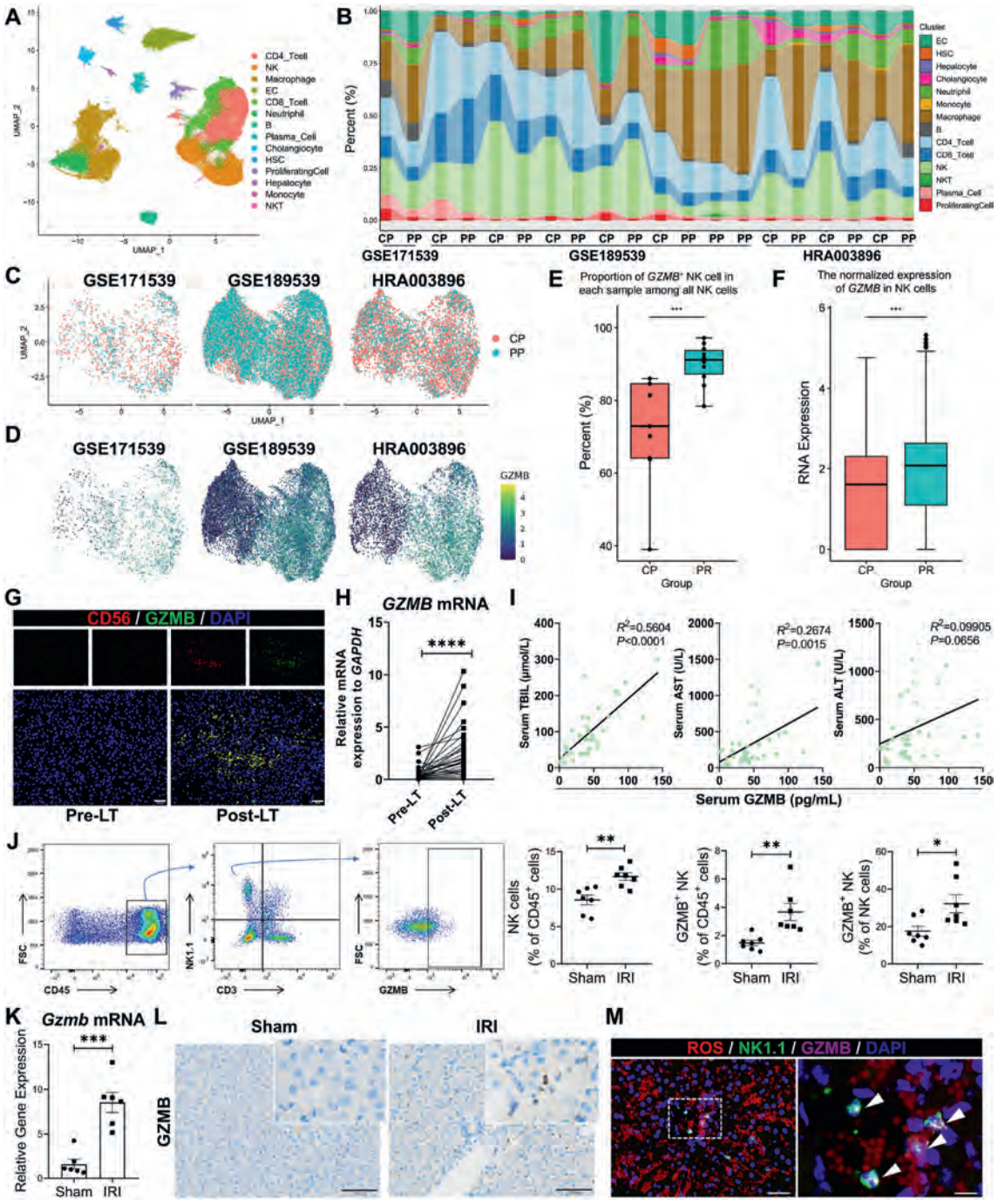

Figure 1 GZMB $^{+}$ NK cells are significantly associated with graft injury in clinical LT samples and the murine hepatic IRI model. (A) UMAP plots displaying a total of 114,705 cells clarified as 14 cell types from 20 samples involving 3 datasets. (B) Cell distribution during the condition of cold preservation (CP) and portal reperfusion (PR). (C) NK cell abundance during the CP and PR phases. (D) Expression of *GZMB* and the distribution of *GZMB*$^{+}$NK cells among NK cells obtained from the three datasets. (E, F) Comparison of *GZMB*$^{+}$NK cells percent and *GZMB* expression between the CP and PR groups in the three datasets, wherein the Wilcoxon test was applied to compare the difference, respectively. (G) Representative immunofluorescence co-staining of NK cells and GZMB in human liver samples collected before and after LT (scale bar = 50 μm). (H) Relative gene expression of *GZMB* to *GAPDH* in human liver before and after transplantation (n = 31). (I) Correlation analysis between the recipient serum level of GZMB and three-day-post-transplant ALT, AST, and TBIL (n = 35). Pearson's correlation was applied to calculate the correlation coefficient between the parameters and corresponding P-values. (J) Flow cytometry analysis of NK cells and GZMB^{+} NK cells among total immune cells in mouse liver from Sham or IRI group (n = 7). (K) Relative mRNA expression of *Gzmb* to β-actin in mouse liver (n = 6). (L) Representative IHC staining of GZMB protein in liver sections (scale bar = 100 μm). (M) Representative images of immunofluorescence co-staining of ROS, NK1.1, and GZMB in mouse liver after IRI (left scale bar = 40 μm, right scale bar = 10 μm, arrow heads indicate co-localization). CP, cold preservation; PR, portal reperfusion; GZMB, granzyme B; NK, natural killer; IRI, ischemia reperfusion injury; ROS, reactive oxygen species. Data are represented as mean ± SEM. *P < 0.05; **P < 0.01; ***P < 0.001; ****P < 0.0001.

($CD45^+CD3^-NK1.1^+$) accumulated within the injured liver tissues as early as 6 h after IRI (Fig. 1J). Flow cytometry further confirmed the augmented proportion of $CD45^+CD3^-NK1.1^+GZMB^+$ cells ($GZMB^+$ NK cells) among the total $CD45^+$ cells and total NK cells at this specific time point following hepatic IRI (Fig. 1J). Notably, the proportion of $GZMB^+$ NK cells among total NK cells in livers peaked at 6 h after reperfusion (Supporting Information Fig. S3). The local activation and degranulation of recruited NK cells were substantiated by the detection of GZMB at both mRNA (Fig. 1K) and protein levels (Fig. 1L). GZMB and NK cells co-localized in regions enriched with reactive oxygen species (ROS), indicating a potentially detrimental role of NK cells in promoting hepatic IRI (Fig. 1M). Furthermore, the presence of GZMB around NK cells suggested active degranulation of NK cells within the infarcted liver tissues. Collectively, these findings demonstrate the recruitment and activation of NK cells within the ischemic liver tissue in a mouse model of hepatic IRI.

3.4. Systemic NK cell depletion significantly reduced intrahepatic GZMB and ameliorated mouse hepatic IRI

To ascertain the role of NK cells during hepatic IRI, we first systemically depleted NK cells using an *in vivo* NK1.1-specific monoclonal antibody (αNK1.1) in mice one week before hepatic IRI (Fig. 2A). The depletion of NK cells did not affect the survival and body weight of mice (Fig. 2B). Flow cytometry analysis confirmed the effective depletion of NK cells in both liver and peripheral blood (Fig. 2C). It is worth noting that systemic NK depletion resulted in a substantial reduction in the population of $CD45^+$ $GZMB^+$ cells ($GZMB^+$ cells) in liver (Fig. 2D) compared to what was previously observed in the IRI group (Supportign Information Fig. S4), indicating that NK cells were the main source of GZMB during the early phase of hepatic IRI. Systemic NK cell depletion also significantly decreased intrahepatic GZMB, as confirmed by both immunofluorescence and ELISA detection in liver tissues, and notably reduced the co-localization with NK cells (Fig. 2E and F). Systemic NK depletion resulted in lower aminotransferase (ALT) and aspartate aminotransferase (AST) after hepatic IRI, indicating reduced hepatocyte injury or even death (Fig. 2G). Infarct size and Suzuki score, assessed by congestion, vacuole degeneration, and necrosis, were also significantly diminished (Fig. 2H). Moreover, systemic NK depletion significantly reduced mRNA levels of *Gzmb* and pro-inflammatory genes *Il-1β*, *Tnf-α,* and tissue injury-related gene *Mmp9* in the liver (Fig. 2I). The consequent reduction of C-CAS3 at the protein level indicated that the improvement in liver function induced by systemic NK cell depletion was associated with the prevention of hepatocyte apoptosis (Fig. 2J). In summary, these findings demonstrate that systemic depletion of NK cells leads to a significant reduction in intrahepatic GZMB, thereby protecting hepatocytes from severe inflammation and lethal apoptosis, ultimately resulting in improved liver function following hepatic IRI.

3.5. Liver-targeted NK cell depletion improved liver function without interfering with NK cells in peripheral blood and other organs

As previously documented, systemic depletion of NK cells is a contentious approach to mitigate hepatic IRI[13,30]. Furthermore, the systemic depletion of NK cells may also impact other organs, thereby potentially disrupting immune responses and leading to tissue damage, particularly in the lungs, where NK cells play a crucial protective role during homeostasis[31,32].

Herein, we have constructed a lipid-based nanoparticle to encapsulate αNK1.1 along with long-circulating polyethylene glycol (PEG), facilitating targeted delivery to the liver (Fig. 3A). The G-LNP/αNK1.1 exhibited an average size of 83 nm, with a narrow size distribution (Fig. 3B). As anticipated, it showed a positive zeta potential of 26.77 mV (Fig. 3C). Capitalizing on the targeted effect, we implemented a reduced dosage of 50 μg/mouse/time for packing αNK1.1 into the nanoparticles, as opposed to the systemic depletion dosage of 100 μg/mouse/time. Following three intravenous administrations of liver-targeted NK1.1 mAb nanoparticles (NK depletion) or an equivalent volume of PBS (NC), we executed the identical hepatic IRI procedure in both groups of mice. Mouse body weights and survival remained unaffected between the two groups (Fig. 3D). Flow cytometry analysis revealed a significant decline in the intrahepatic proportion of total NK cells following depletion (Fig. 3E). However, NK cells were not affected in the peripheral blood between the two groups (Fig. 3F). IHC staining of NK1.1 in liver and other organ tissues confirmed a lower ratio of NK cell infiltration in the liver, but no significant difference was observed among the spleens, hearts, lungs, and kidneys (Fig. 3G). Consistently, both IHC and ELISA measurements demonstrated markedly lower levels of intra-hepatic GZMB in the NK depletion group (Fig. 3H and I). Following hepatic IRI, a significantly lower level of plasma ALT, AST, and TBIL was detected in the liver-targeted NK depletion group, indicating reduced hepatocyte injury and improved liver function (Fig. 3J). HE staining between the two groups demonstrated more severe tissue injury in the NC group, as assessed by higher Suzuki scores (Fig. 3H). A lower level of hepatocyte apoptosis after liver-targeted NK depletion was demonstrated after IRI (Fig. 3H and K). These results lead us to the conclusion that liver-targeted NK cell depletion improves liver function after hepatic IRI without interfering with NK cells in peripheral blood and other organs. Moreover, it is possible to achieve a comparatively protective effect with a reduced dosage of anti-NK1.1 mAb.

3.6. Gzmb-deficient NK cells failed to affect liver injury and function after hepatic IRI

To further validate the role of NK cell-derived GZMB, $Il2rg^{-/-}Rag2^{-/-}$ (B6RG) mice lacking T, B, and NK cells were subjected to different treatments. They were either injected with PBS (NC) or received adoptive transfer of NK cells isolated from spleenocytes of C57BL/6 WT mice (WT-NK) or *Gzmb*-KO mice (KO-NK) for 5 days of amplification *in vivo*, prior to hepatic IRI (Fig. 4A). The genotyping of *Gzmb*-KO strains was shown in Supporting Information Fig. S1. The purity of isolated NK cells exceeded 90% (Supporting Information Fig. S5). Initially, we confirmed that re-supplementation with either WT or *Gzmb*-KO NK cells significantly increased the number of NK cells in the spleens and livers of B6RG mice, compared to mice injected with PBS alone. There was no significant difference observed between the two groups receiving adoptive transfer (Fig. 4B and C). However, GZMB expression was highly pronounced in mice that received WT NK cells, but decreased after the transfer of *Gzmb*-KO NK cells (Fig. 4C). Subsequently, we examined the consequences of *Gzmb* deficiency in NK cells on post-ischemic liver injury. The transfer of WT NK cells into

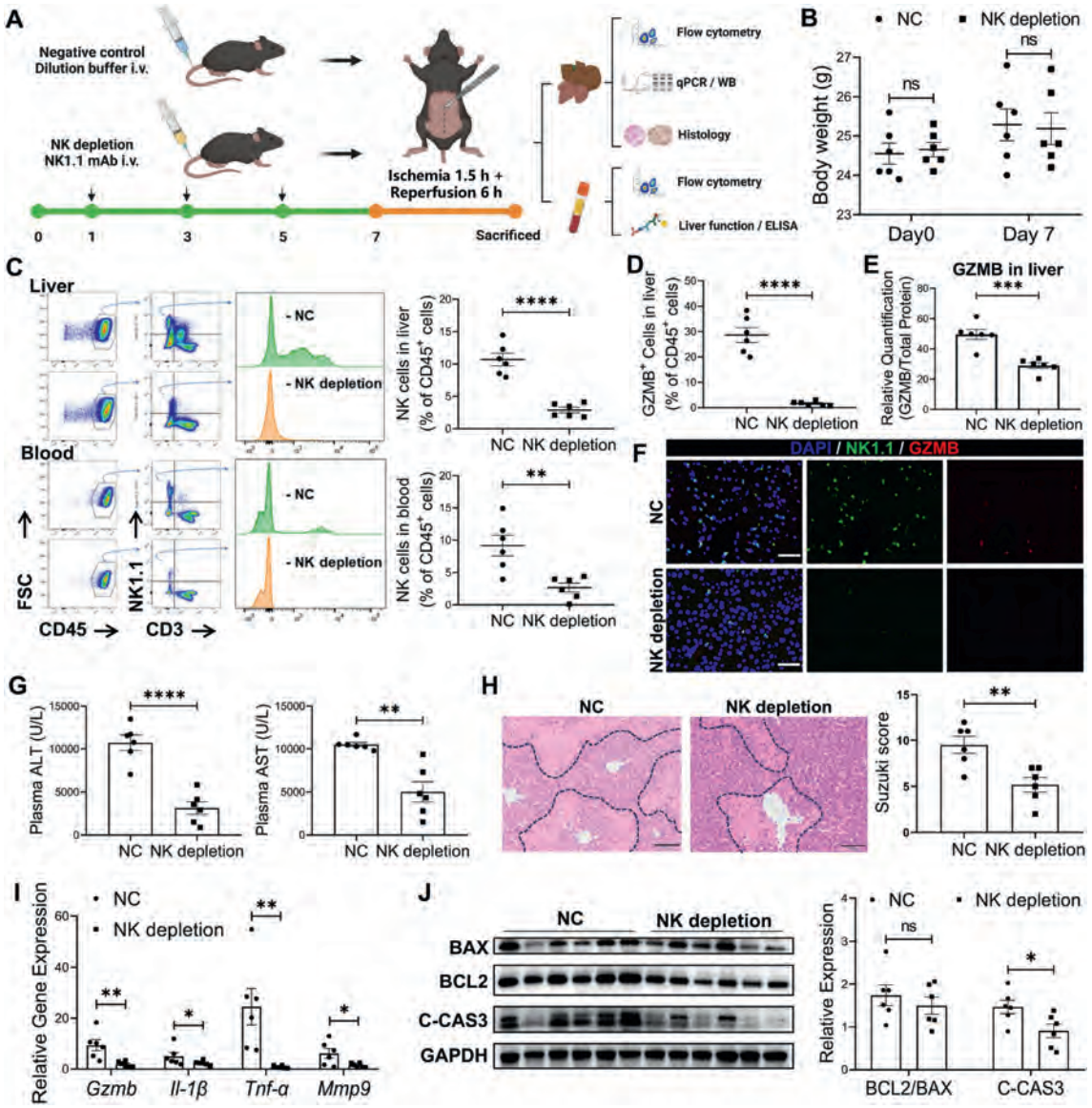

Figure 2 Systemic NK depletion attenuates hepatic IRI *in vivo*. (A) Schematic image of experiments ($n = 6$). (B) Body weight record of the mouse receiving NK1.1 mAb or control a week before hepatic IRI. (C) Flow cytometry analysis of NK cells among total CD45$^+$ cells in liver and blood, respectively. (D) Flow cytometry analysis of total GZMB$^+$ cells among total CD45$^+$ cells in the liver. (E) Intra-hepatic tissue level of GZMB measured by ELISA and relatively quantified by total protein concentration. (F) Representative immunofluorescence staining of NK1.1 and GZMB in liver (scale bar = 50 μm). (G) Plasma level of ALT and AST. (H) Representative images of HE staining of mouse liver and analysis of Suzuki score (scale bar = 100 μm). (I) Relative mRNA expression of *Gzmb*, *Il-1β*, *Tnf-α*, and *Mmp9* to β-actin in mouse liver. (J) Relative protein level of BAX/BCL2 and cleaved caspase3 (C-CAS3) in mouse liver. GZMB, granzyme B; NK, natural killer; NC, negative control. Data are represented as mean ± SEM. *$P < 0.05$; **$P < 0.01$; ***$P < 0.001$; ****$P < 0.0001$; ns, not significant.

B6RG mice aggravated liver function after hepatic IRI, in comparison to the NC group. However, this detrimental effect was reversed when *Gzmb*-KO NK cells were transferred (Fig. 4D). Necrotic areas and Suzuki score of liver tissues were significantly increased in the WT-NK group, but this pathogenic effect was nullified after re-supplementation with *Gzmb*-KO NK cells (Fig. 4C). After transferring *Gzmb*-KO NK cells, the levels of *Il-1β*, *Tnf-α,* and *Mmp9* mRNA in the liver were notably diminished following IRI, indicating a less severe inflammatory response and tissue damage (Fig. 4E). The presence of intra-hepatic apoptosis was confirmed through IHC staining and the relative quantification of apoptosis-related proteins. Remarkably, the adoptive transfer of *Gzmb*-KO NK cells provided significant protection to the mouse liver against apoptosis when compared to the transfer of WT NK cells (Fig. 4C and F). The above results underscore the pivotal role of NK cells in the initiation of hepatic IRI, while emphasizing their inability to influence liver function in the absence of GZMB.

In order to clarify the mechanism of GZMB inhibition reducing hepatocyte apoptosis and pro-inflammatory responses, we performed mouse hepatocyte hypoxia/reoxygenation (Hypoxia: 1% O_2, 5% CO_2; Reoxygenation: 21% O_2, 5% CO_2) experiments to

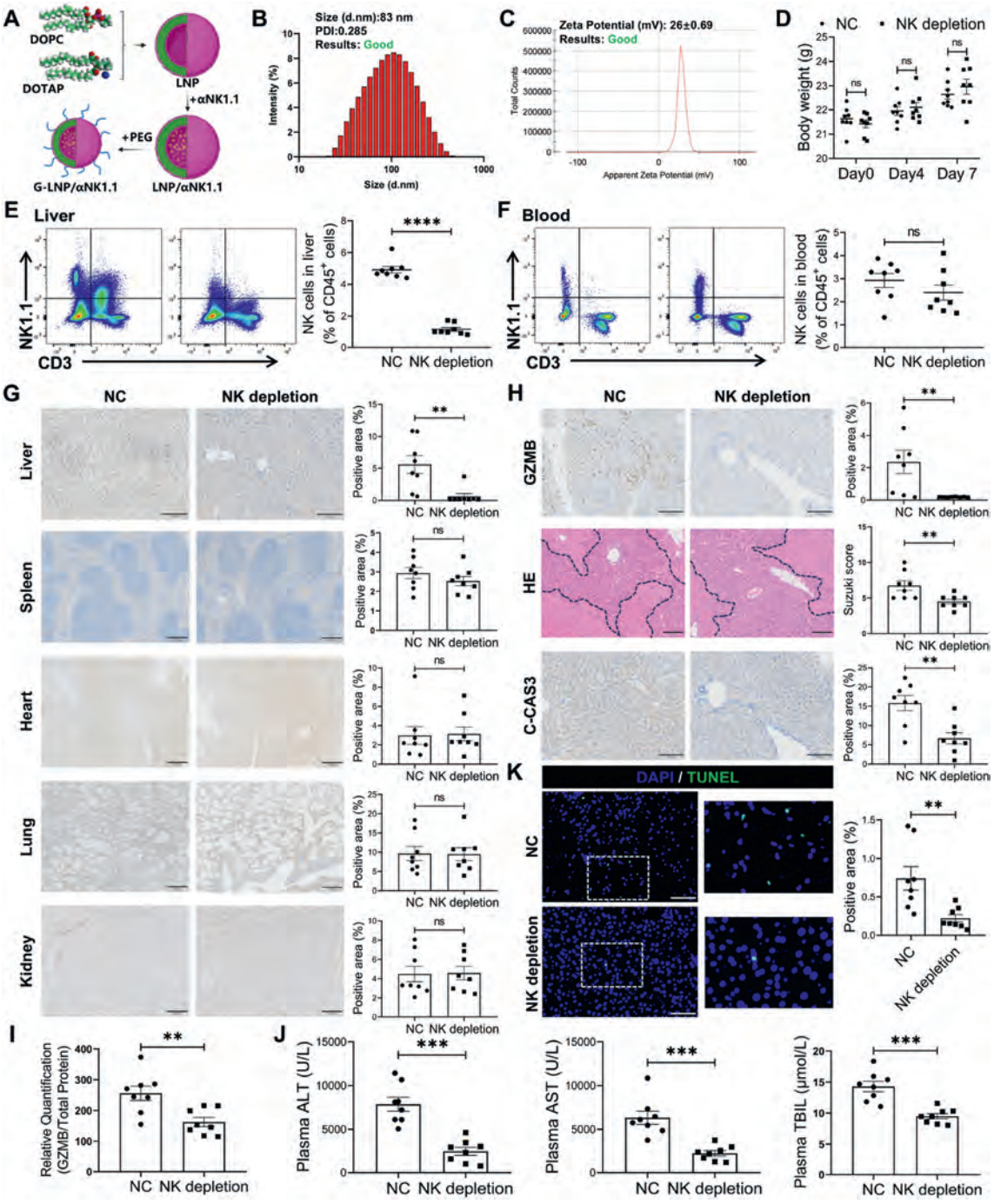

Figure 3 Nanoparticle delivery system, assisting liver-targeted NK depletion, attenuates hepatic IRI with increased efficiency. (A) Illustration of the fabrication of αNK1.1 nanoparticles. (B) The optimized size distribution of the nanoparticles was determined by dynamic light scattering. (C) The representative zeta potential of the nanoparticles was determined by dynamic light scattering. (D) Body weight record of a mouse receiving liver-targeted NK depletion a week before hepatic IRI. ($n = 8$). (E) Flow cytometry analysis showing total NK cells among total $CD45^+$ cells in the liver between the two groups. (F) Flow cytometry analysis showing total NK cells among total $CD45^+$ cells in blood between the two groups. (G) Representative images of IHC for NK1.1 staining of mouse liver, spleen, heart, lung, and kidney from NC and liver-targeted NK depletion group (scale bar = 100 μm). (H) Representative images of HE staining (scale bar = 100 μm), and IHC for GZMB and cleaved caspase3 (C-CAS3) (scale bar = 100 μm). (I) Intra-hepatic tissue level of GZMB measured by ELISA and relatively quantified by total protein concentration. (J) Plasma level of ALT, AST, and TBIL. (K) Representative images of immunofluorescence staining of TUNEL in liver (scale bar = 100 μm). DOPC, 1,2-dioleoyl-*sn*-glycero-3-phosphocholine ($C_{44}H_{84}NO_8P$); DOTAP, 1,2-dioleoyl-3-trimethylammonium-propane (chloride salt) ($C_{42}H_{80}NO_4Cl$); LNP, liposome nanoparticles; PDI, polydispersity index; GZMB, granzyme B; NK, natural killer; NC, negative control. Data are represented as mean ± SEM. $^{**}P < 0.01$; $^{***}P < 0.001$; $^{****}P < 0.0001$; ns, not significant.

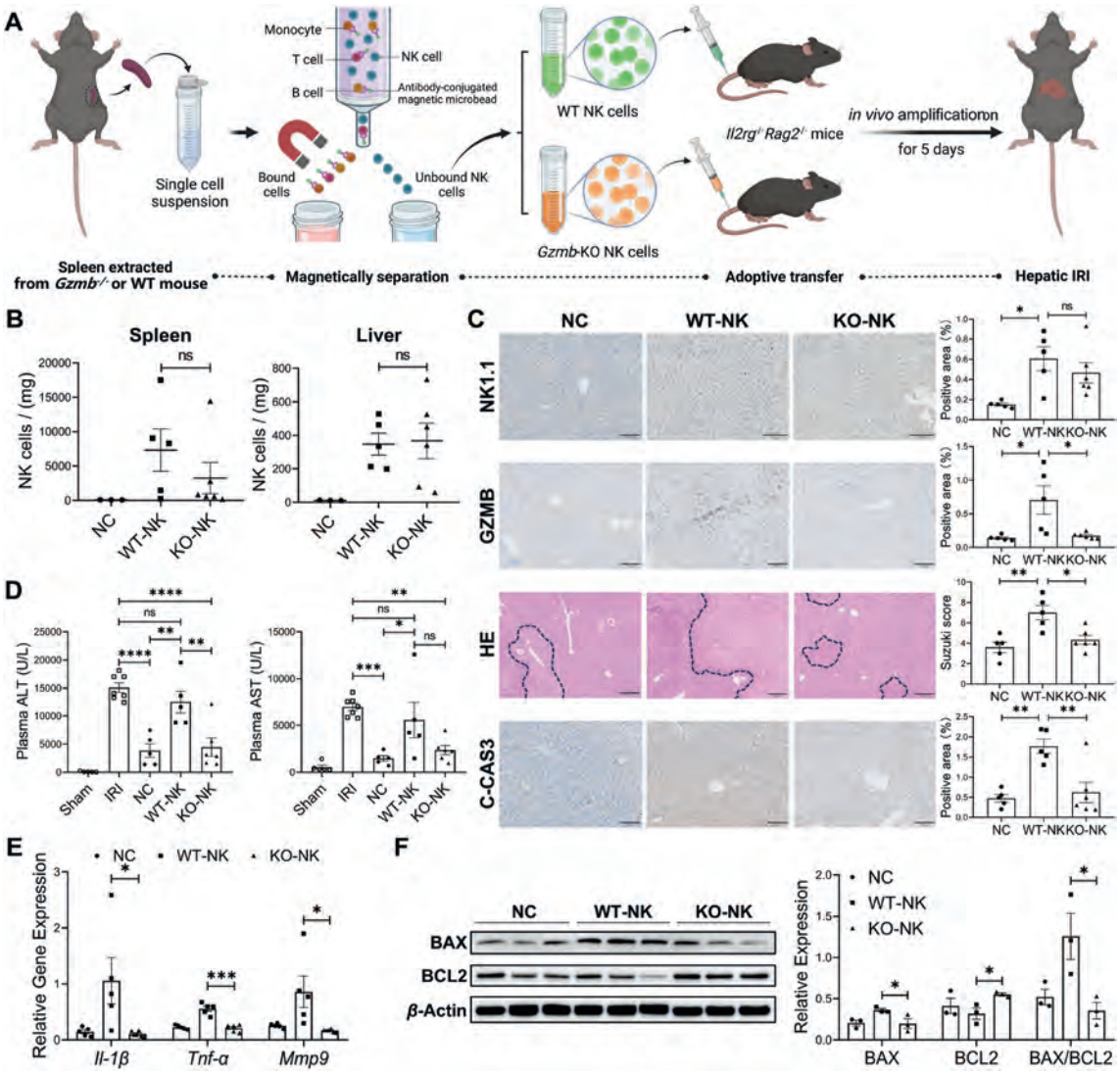

Figure 4 NK cells trigger hepatocyte apoptosis and deteriorate liver function through the production of GZMB. (A) Experimental process of NK cells adoptive transfer and murine hepatic IRI model. (B) Absolute quantification of NK cells in spleens and livers after hepatic IRI from immunodeficient or adoptively transferred mice (NC, $n = 3$; WT-NK, $n = 5$; KO-NK, $n = 6$). (C) Representative images of HE staining (scale bar = 200 μm, dashed lines delineate the necrotic areas) and IHC for NK1.1, GZMB, and cleaved caspase3 (C-CAS3) (NC, $n = 5$; WT-NK, $n = 5$; KO-NK, $n = 6$) (scale bar = 100 μm). (D) Mouse plasma level of ALT and AST (Sham, $n = 5$; IRI, $n = 7$; NC, $n = 5$; WT-NK, $n = 5$; KO-NK, $n = 6$). (E) Relative mRNA expression of *Il-1β*, *Tnf-α* and *Mmp9* to β-actin in mouse liver (Sham, $n = 5$; IRI, $n = 7$; NC, $n = 5$; WT-NK, $n = 5$; KO-NK, $n = 6$). (F) Relative protein level of BAX, BCL2, and C-CAS3 measured by Western blot ($n = 3$). GZMB, granzyme B; NK, natural killer; IRI, ischemia reperfusion injury; NC, negative control; WT, wildtype; KO, knockout; *Il-1β,* interleukin-1β; *Tnf-α*, tumor necrosis factor α; *Mmp9*, metalloproteinase 9. Data are represented as mean ± SEM. $^{*}P < 0.05$; $^{**}P < 0.01$; $^{***}P < 0.001$; $^{****}P < 0.0001$; ns, not significant.

investigate the underlying mechanisms of GZMB inducing hepatocyte apoptosis, which supplemented the culture medium with recombinant mouse GZMB protein (rmGZMB) when reoxygenating to simulate the GZMB released by NK cells during portal reperfusion in liver transplantation (Supporting Information Fig. S6A). As shown below, either low (10 nmol/L) or high (100 nmol/L) concentration of rmGZMB could significantly induce hepatocyte apoptosis (Fig. S6B). Furthermore, we performed RNA-seq to investigate the majorly affected transcription between the NC and GZMB-High groups ($n = 3$ each group). Compared with the NC group, 271 significantly upregulated and 201 significantly downregulated genes were identified in the GZMB-treating group (Fig. S6C and S6D). GO analysis identified that the differently expressed genes (DEGs) were mainly enriched in the regulation of gene transcription, mitochondrial respiration, and extracellular matrix, which have exerted critical roles in liver graft injury during transplantation (Fig. S6E). Furthermore, GSEA analysis has confirmed the down-regulation of these pathways after GZMB treatment, as well as the activation of apoptotic signaling pathways and innate immune response (Fig. S6F). Together, these results revealed the underlying mechanisms of GZMB inducing apoptosis and pro-inflammatory responses in liver IRI.

3.7. Global Gzmb deficiency reduced liver damage after IRI

Next, we examined the direct cytotoxic impact of GZMB on liver injury following ischemia. The induction of hepatic IRI was carried out in adult mice of the C57BL/6 wildtype (WT) and global *Gzmb*-deficient (*Gzmb*-KO) strains. Intrahepatic *Gzmb* deficiency was confirmed at the mRNA and protein levels before surgery (Fig. 5A and B). A notable decrease in ALT and AST levels was observed in *Gzmb*-KO mice compared to the WT group after hepatic IRI (Fig. 5C). The gene expression of *Il-1β*, *Tnf-α,* and *Mmp9* was significantly lower, indicating a milder degree of liver injury in *Gzmb*-KO mice (Fig. 5D). Following hepatic IRI, infiltration of NK cells was observed in the injured liver of both WT and *Gzmb*-KO mice (Supporting Information Fig. S7), but significantly lower levels of GZMB were detected in *Gzmb*-KO mice (Fig. 5E). The necrotic areas in liver tissues and the corresponding Suzuki score of *Gzmb*-KO mice were lower than those of WT mice (Fig. 5E). Immunohistology staining of C-CAS3 (Fig. 5F) and immunofluorescence staining of TUNEL in liver tissues (Fig. 5E) revealed a local reduction in hepatocyte apoptosis. Notably, the co-localization of GZMB and TUNEL indicated that the majority of hepatocyte apoptosis was caused by the cytotoxicity of GZMB (Fig. 5E). Altogether, our findings suggest that global *Gzmb* deficiency limits liver damage following IRI in mice.

3.8. GZMB inhibition reduced hepatocyte apoptosis and pro-inflammatory responses in the murine hepatic IRI model

These findings have led us to consider inhibiting the direct cytotoxic role of GZMB in hepatic IRI. Initially, mice were administered an irreversible serine protease inhibitor, AEBSF, *via* peritoneal injection at a dose of 80 mg/kg body weight at different time points prior to IRI (Fig. 6A and Supporting Information Fig. S8). In order to confirm the selectivity and specificity of AEBSF in inhibiting GZMB, surface plasmon resonance (SPR) was performed to measure the interaction affinity of AEBSF with mouse GZMB protein using Biacore, which was determined by means of a CM5 chip-coupled protein (Supporting Information Fig. S9 and Supporting Information Table S4). The results showed that the dissociation constant (K_D) between mouse GZMB and AEBSF was 5.49E-06, indicating that the affinity of AEBSF to the mouse GZMB protein is strong, since the reference value of K_D between protein and small molecules is 10^{-3}−10^{-6} mol/L, and the smaller the value, the stronger the affinity. Therefore, the selectivity and efficacy of AEBSF in inhibiting mouse GZMB were reliable.

By comparing the serum levels of ALT and AST among different groups, we observed that only injection 1 h before surgery significantly reduces liver injury (Fig. 6B and Supporting Information Fig. S8). GZMB was significantly decreased in both serum and tissue levels after hepatic IRI (Fig. 6C). This inhibition was further confirmed at the protein level by IHC staining of liver tissues (Fig. 6D). HE staining revealed a substantial reduction in necrotic tissue area and Suzuki score in mice pre-treated with AEBSF (Fig. 6D). Surprisingly, the proportion of total NK cells and GZMB $^+$ NK cells also declined in the IRI + AEBSF group, potentially as a secondary effect of reduced liver injury, which recruited and activated fewer NK cells in the liver (Supporting Information Fig. S10). Of note, the mRNA levels of *Il-1β*, *Tnf-α,* and *Mmp9* were significantly lower in the injured liver of IRI + AEBSF mice compared to the control group (Fig. 6E). Furthermore, intrahepatic apoptosis was notably decreased after pharmacological inhibition of GZMB (Fig. 6F and G). These findings underscore the protective function of GZMB inhibition in mitigating intrahepatic apoptosis and inflammation in hepatic IRI.

3.9. GZMB inhibition improved liver function and reduced hepatocyte apoptosis in rats after LT

Next, we sought to investigate whether GZMB inhibition could also mitigate liver injury in rats after LT. To achieve this, AEBSF was administered *via* peritoneal injection at a dose of 60 mg/kg to 6 recipient rats 6 h prior to transplantation (LT + AEBSF). In contrast, another 12 rats received an equivalent volume of PBS (Sham = 6 and LT + PBS = 6 recipients). Liver tissues and blood samples were collected 24 h after LT (Fig. 6H). The serum levels of ALT and AST in the post-transplantation period were significantly lower in rats pre-treated with AEBSF (Fig. 6I), indicating reduced liver injury, as confirmed by HE staining (Fig. 6J). IHC staining of GZMB demonstrated effective inhibition, and the intra-hepatic level of apoptosis was markedly decreased, as evidenced by a reduction in the positive areas of C-CAS3 in the LT + AEBSF group (Fig. 6J). Together, these results demonstrated that GZMB inhibition improved liver function and reduced hepatocyte apoptosis in rats following LT.

3.10. FDA-approved drugs screening for potential GZMB inhibition to reduce hepatic IRI in vivo

Furthermore, we performed molecular dynamics simulations based on FDA-approved drugs in order to screen for a potent and clinically safe GZMB inhibitor. Mouse GZMB, as a serine protease, has a catalytic pocket to bind substrate and a conserved serine residue inside the pocket (upper panel of Fig. 7A). A recent work performed an extensive theoretical study to scan FDA-approved drugs and their derivatives for finding inhibitors against human GZMB, and several molecules as inhibitor candidates were shown[33]. On the other hand, we also noted previous publications have pointed out that, due to differences of some critical residues between human and mouse GZMB, it is not self-evident that an inhibitor against one GZMB can inhibit the other one as well[34]. Therefore, molecular docking and dynamics simulations were carried out to predict interactions of mouse GZMB with these candidates (*i.e.*, tannic acid, mupirocin, cefpiramide, xenazoic acid, and vidarabine phosphate).

Firstly, these candidates were, respectively, docked into the pocket of mouse GZMB. In each docking, the top three poses of the small molecule according to the ranking score were selected. Then, each pose of these molecules in complex with mouse GZMB was submitted to at most 1000 ns MD simulations. As a result, only vidarabine phosphate (Vida, lower panel of Fig. 7A) remained bound in mouse GZMB's pocket during all simulations, implying a strong interaction between them. Incidentally, vidarabine phosphate, which has an antiviral effect, is the monophosphorylated molecule of the FDA-approved drug vidarabine[35].

Further, a detailed analysis was conducted to study the mechanism behind the strong binding. The curve in Fig. 7B is the distance between Vida's phosphate group and Ser203's hydroxyl group in the simulation trajectory. We plotted in Fig. 7C the electrostatic potential surface of the protein. Our additional calculations (not shown here) found that vidarabine cannot bind stably to the protein. They together lead to the conclusion that the phosphate group plays a critical role in the binding. At last, the interaction energy between

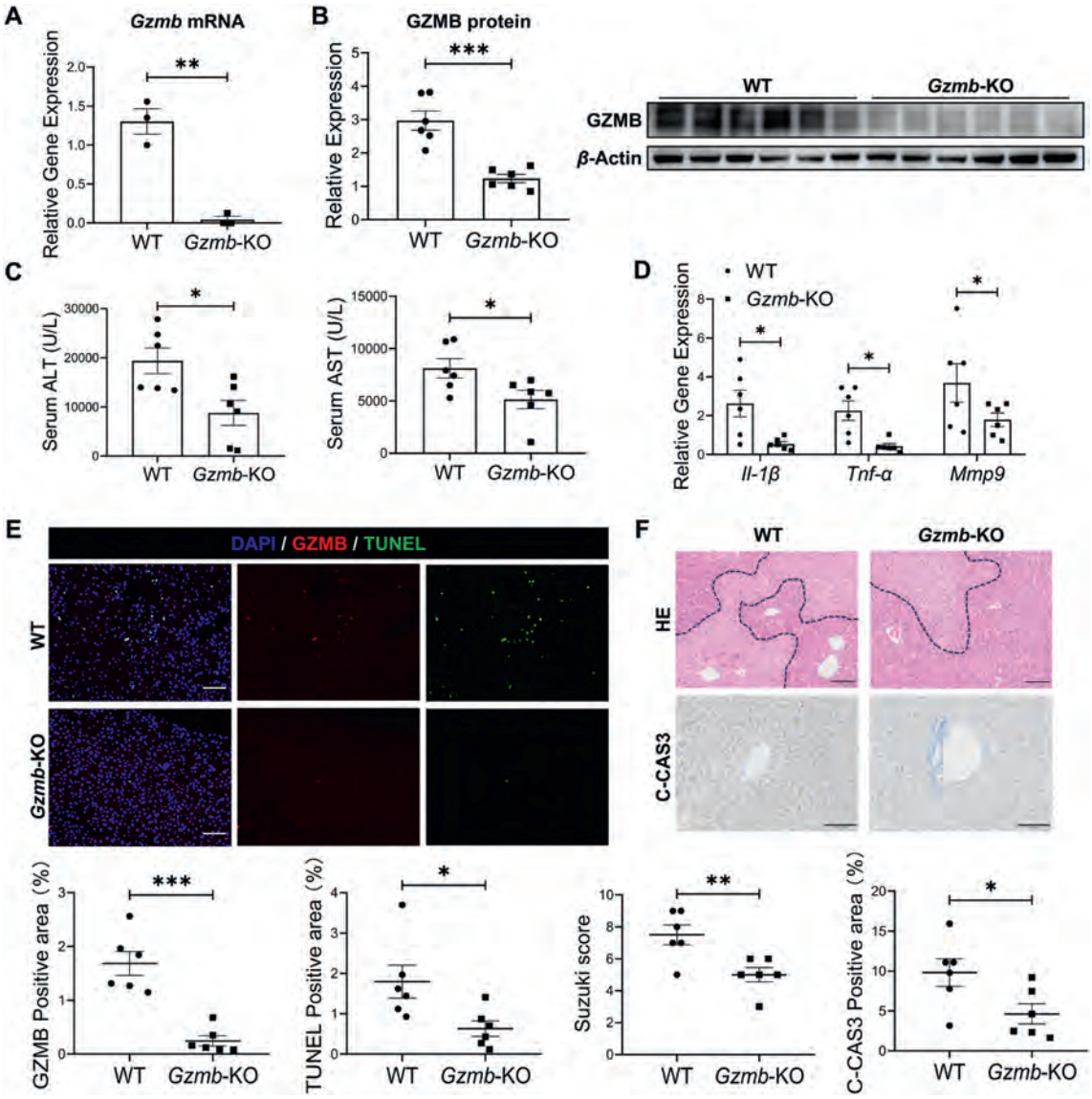

Figure 5 Global *Gzmb* deficiency alleviates hepatic IRI. (A) Relative gene expression of Gzmb to β-actin in mouse liver tissues ($n = 3$). (B) Relative protein expression of GZMB in mouse liver tissues ($n = 6$). (C) Mouse serum level of ALT and AST ($n = 6$). (D) Relative gene expression of *Il-1β*, *Tnf-α*, and *Mmp9* to β-actin in mouse liver tissues ($n = 6$). (E) Representative images of immunofluorescence staining of GZMB and TUNEL in liver (scale bar = 100 μm) ($n = 6$). (F) Representative images of HE staining of mouse livers (scale bar = 100 μm), and IHC for C-CAS3 (scale bar = 100 μm) ($n = 6$). GZMB, granzyme B; WT, wild type; KO, knockout. Data are represented as mean ± SEM. $^*P < 0.05$; $^{**}P < 0.01$; $^{***}P < 0.001$.

vidarabine phosphate and mouse GZMB was calculated (Fig. 7D). This quantitatively confirms that the electrostatic interaction plays a dominant role in the binding. In order to confirm the selectivity and specificity of Vida in inhibiting GZMB, SPR was also performed to measure the interaction affinity (Supporting Information Fig. S9 and Supporting Information Table S4). The results showed that the dissociation constant (K_D) between mouse GZMB and Vida was 2.38E-06, indicating that the affinity of Vida to the mouse GZMB protein is strong, and the selectivity and efficacy were also reliable.

To assess the efficacy of vidarabine phosphate in mitigating hepatic IRI, mice were randomly assigned to either the sham or hepatic IRI groups (NC, hepatic IRI pre-treated with PBS; Vida, hepatic IRI pre-treated with vidarabine phosphate; Cyta, hepatic IRI treated with cytarabine to avoid interference from the antiviral drug's effects) (Fig. 7E). Following hepatic IRI, there was no significant difference in the serum levels of GZMB among the three groups (Fig. 7F), but a notable reduction in GZMB accumulation was observed in the liver tissues of the Vida group (Fig. 7G and H). Correspondingly, the levels of serum ALT and AST were significantly lower in the Vida group compared to the other IRI groups, indicating its potential in improving liver function post-hepatic IRI (Fig. 7I). Mice pre-treated with vidarabine phosphate exhibited significantly reduced liver injury, while no difference was observed between the NC and Cyta groups (Fig. 7H). Furthermore, the relative gene expression of *Il-1β*, *Tnf-α,* and *Mmp9* indicated a milder inflammatory response associated with GZMB inhibition in the Vida group following hepatic IRI (Fig. 7J). Intrahepatic apoptosis was also decreased in the Vida group (Fig. 7H and K).

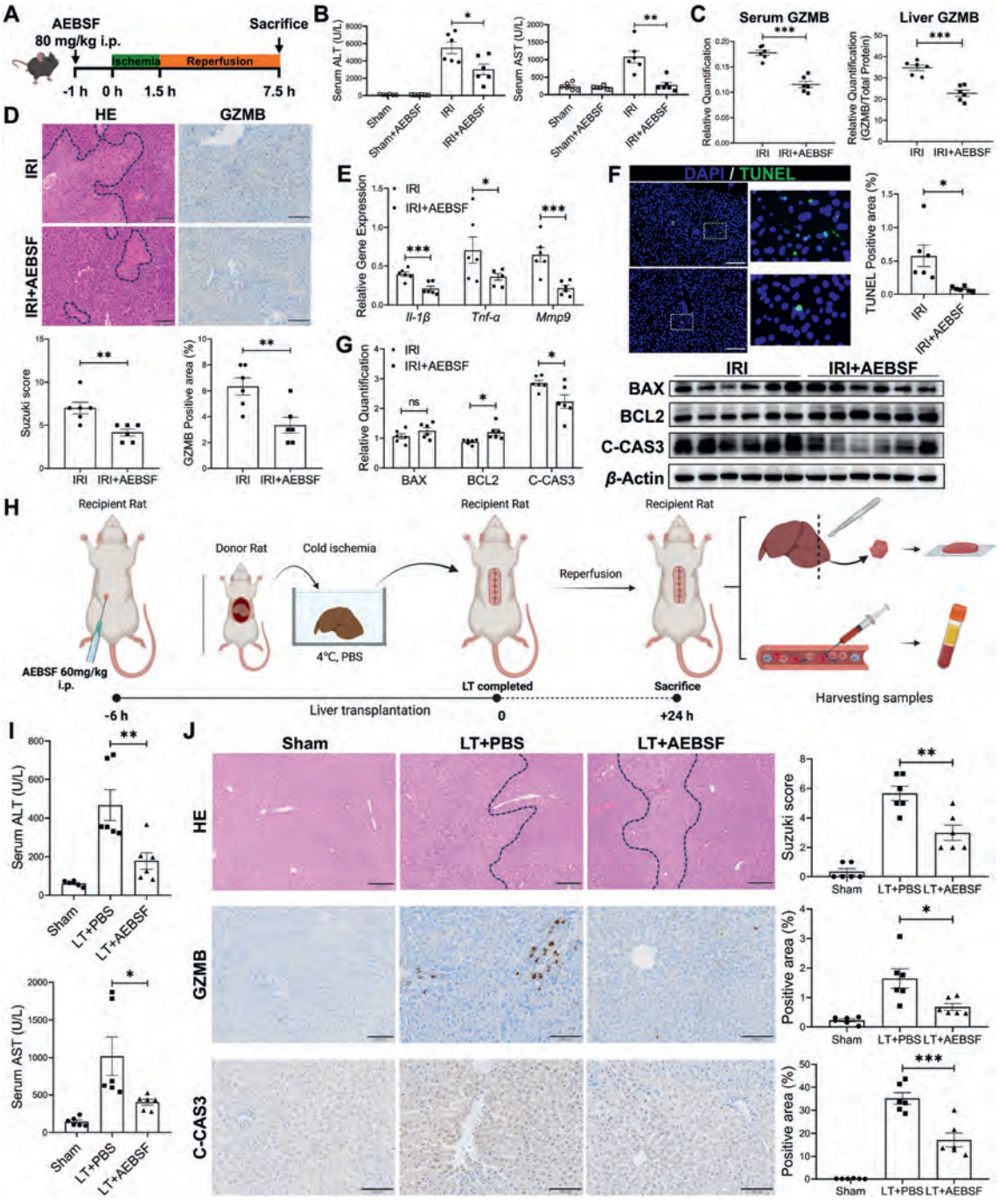

Figure 6 AEBSF inhibits GZMB and improves liver function in both murine hepatic IRI and rat LT model (A) Schematic image of the experiments ($n = 6$). (B) Mouse serum levels of ALT and AST. (C) Relative quantification of GZMB in serum and liver by ELISA. (D) Representative images of HE staining (scale bar = 100 μm, dashed lines delineate the necrotic areas) and IHC for GZMB (scale bar = 100 μm) in mouse liver. (E) Relative gene expression of *Il-1β*, *Tnf-α*, and *Mmp9* to *β-actin* in mouse liver tissues. (F) Representative images of immunofluorescence staining of TUNEL in mouse liver (scale bar = 100 μm). (G) Relative protein level of BAX, BCL2, and cleaved caspase3 (C-CAS3) measured by Western blot. (H) Schematic image of rat LT experimental process ($n = 6$). (I) Rat serum levels of ALT and AST. (J) Representative images of HE staining (scale bar = 200 μm, dashed lines delineate the necrotic areas), and IHC for GZMB and C-CAS3 (scale bar = 100 μm) in rat livers. LT, liver transplantation; GZMB, granzyme B; C-CAS3, cleaved caspase3. Data are represented as mean ± SEM. $^{*}P < 0.05$; $^{**}P < 0.01$; $^{***}P < 0.001$; ns, not significant.

Collectively, these findings highlight the potential of vidarabine phosphate as a therapeutic intervention for ameliorating graft injury through the inhibition of GZMB during the process of LT.

Moreover, we have also tried to apply Vida in the rat LT model, expecting to improve graft function with this FDA-approved drug. However, the pre-treatment of Vida did not reduce liver injury in

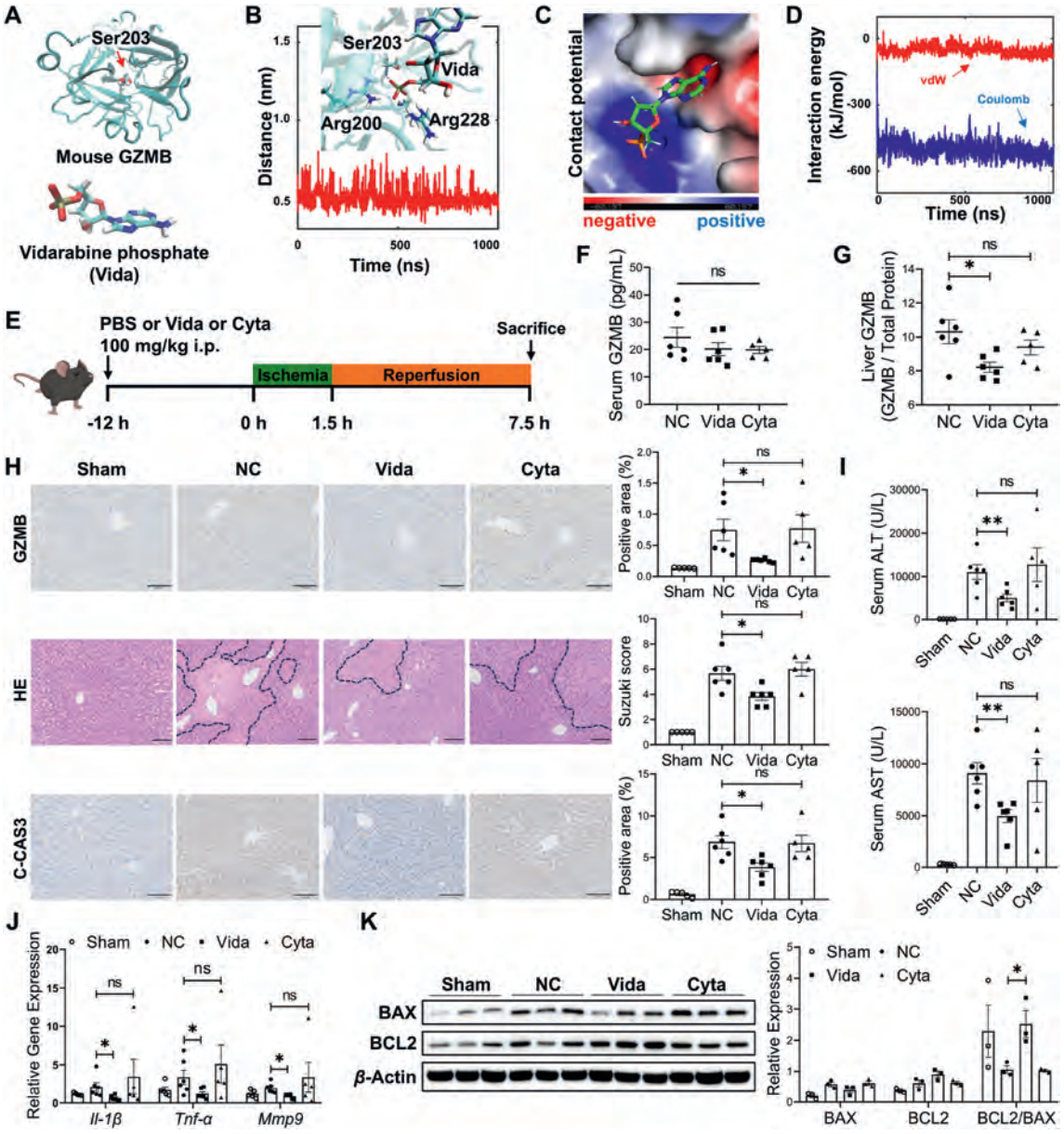

Figure 7 FDA-approved vidarabine phosphate functions as a potent GZMB inhibitor to reduce hepatic IRI. (A) 3D structure of mouse GZMB protein and small molecule Vida, wherein the active site Ser203 inside the catalytic pocket of mouse GZMB and Vida are both in stick representations. (B) Time-dependent distance between the phosphate group of Vida and the hydroxyl group of Ser203. Inset: An MD simulation snapshot of Vida in complex with mouse GZMB. (C) The contact potential surface of mouse GZMB, blue (red), represents positive (negative) contact potential. (D) Time evolution of interaction energy between vidarabine phosphate and mouse GZMB. In all the stick representations in (A−C), yellow indicates phosphorus atoms, red oxygen atoms, green carbon atoms, blue nitrogen atoms, and white hydrogen atoms. (E) Schematic image of the experiments (Sham, Cyta, $n = 5$; NC, Vida, $n = 6$). (F) Quantification of GZMB in mouse serum and liver by ELISA. (G) Intra-hepatic tissue level of GZMB measured by ELISA and relatively quantified by total protein concentration. (H) Representative images of IHC for GZMB and cleaved caspase3 (C-CAS3) (scale bar = 100 μm) and HE staining (scale bar = 100 μm, dashed lines delineate the necrotic areas). (I) Mouse serum levels of ALT and AST. (J) Relative mRNA expression of *Il-1β*, *Tnf-α*, and *Mmp9* to β-actin in mouse liver. (K) Relative protein level of BAX, BCL2, and C-CAS3 measured by Western blot ($n = 3$). GZMB, granzyme B; NK, natural killer; IRI, ischemia reperfusion injury; NC, negative control; Vida, vidarabine phosphate; Cyta, cytarabine; *Il-1β*, interleukin-1β; *Tnf-α*, tumor necrosis factor α; *Mmp9*, metalloproteinase 9. Data are represented as mean ± SEM. $^*P < 0.05$; $^{**}P < 0.01$; ns, not significant.

recipient rats compared to the control (Supporting Information Fig. S11A and S11B). Intra-hepatic level of GZMB was also similar between the two groups, which indicated that Vida may not be able to bind and inhibit rat GZMB protein since we previously screened only in docking with mouse GZMB (Fig. S11B). Next, we carried out theoretical studies (molecular docking and dynamics

simulations) to investigate the interaction between rat GZMB protein and Vida, trying to recover the molecular mechanism behind the different responses of mouse/rat GZMB proteins upon Vida treatments. Fig. S11C and S11D display representative conformations of mouse/rat GZMB proteins when interacting with Vida (Vida is not shown for visual clarity). The sequence from 220 to 230 of mouse protein is GYKDGSPPRAF, while the corresponding sequence in the rat case is GQNDGSTPRAF. The different parts between them are rendered in yellow. It can be found that in the mouse case, this segment bends strongly to expose residue R200. The exposed R200 plus R228 together form a positively charged pocket to accommodate negatively charged Vida and therefore tightly block the active site S203. In contrast, in the rat case, this segment forms a loose loop, which buries R201 inside the protein. This leads to Vida interacting with R229 only and binding to a region relatively far from the active site S204. This difference is explicitly shown through calculated distances between Vida and active sites in the two cases (Fig. S11E). The theoretical results presented here support our experimental finding that, compared with mouse GZMB, Vida cannot interrupt the catalytic function that is observed in the rat case. And also, Vida could not improve rat liver function under these circumstances, which partially emphasized the critical role of GZMB in inducing liver graft injury.

4. Discussion

Hepatic IRI is a complex process including hypoxia-induced damage and sterile inflammation mediated by immune homeostasis imbalance[36]. Innate immune cells, including Kupffer cells and neutrophils, have been reported as the first responders to damage-related molecular patterns[37,38]. In this study, single-cell transcriptomics has pinpointed $GZMB^+$ NK cells as notably prevalent infiltrates in post-transplant human livers. Consistently, Arias-Diaz et al.[39] have also demonstrated a significant increase in NK cell infiltration in rat hepatic IRI models. NK cells play a critical role in anti-viral[9] and anti-tumor responses[40], but their role in hepatic IRI remains unclear[11]. Previous studies have shown that depletion of NK cells can significantly reduce the secretion levels of liver inflammatory factors (TNF-α, IL-1b, IL-6, IL-8, and CXCL-2) and reduce early neutrophil infiltration in hepatic IRI[30,41]. However, it has also been reported that NK cell depletion may not affect liver function[13,42], and RORγt(+) IL-22-producing NK cells could even exert a protective role during hepatic IRI[43]. Therefore, further investigation in NK cells should focus on different subgroups with diverse biomarkers, which may function adversely in the same process.

By combining "loss of function" using NK cell-depleting treatment with anti-NK1.1 mAb and a "gain of function" strategy based on NK cell supplementation in *Il2rg*$^{-/-}$*Rag2*$^{-/-}$ mice, we demonstrated that NK cells promote deleterious post-IRI liver injury in a GZMB-dependent manner. GZMB has been previously identified as a major toxic protein in cancer and auto-immune diseases like diabetes and cardiovascular diseases, such as stroke[44,45]. Referring to cardiac transplantation, GZMB may promote inflammatory responses and allograft rejection, thus affecting long-term graft survival[46]. GZMB inhibition by serine protease inhibitor-6 has been reported to reduce injury of renal tubular cells and promote renal allograft survival[47]. In the context of hepatic IRI, GZMB was detected in the damaged area at early time points and co-localized with infiltrating NK cells and $TUNEL^+$ cells. Genetic and pharmacological inhibition of GZMB has improved liver function in both murine hepatic IRI and rat LT models.

It is worth noting that NK cells and their derived GZMB were detected in human liver tissues after LT, and recipients with high serum levels of GZMB within 2 h of liver reperfusion were associated with an increased risk of post-transplant liver dysfunction. Although T cells may also express GZMB to enhance the cytotoxicity, the single-cell sequencing data analysis has revealed that GZMB expression was significantly higher in NK cells (Fig. S2). Moreover, research from our team has recently shown that the proportion of circulating NK cells may be related to EAD after LT[48]. Therefore, it is possible to speculate that serum levels of GZMB could serve as a biomarker to identify patients who may benefit from anti-NK-depleting antibodies in hepatic IRI.

However, depleting NK cells in patients as a clinical intervention to prevent organ injury may raise safety concerns, including pneumonia and infection[49-51]. Instead, switching to strategies that inhibit GZMB in patients appears to be more feasible. By referencing a screening project of FDA-approved drugs to find potential inhibitors against human GZMB, we performed molecular dynamic simulations between the candidates and mouse GZMB, and identified vidarabine phosphate as the most promising drug to inhibit mouse GZMB *in vivo*. Notably, we did observe a protective role of vidarabine phosphate in mouse hepatic IRI.

There are some limitations in our study. Firstly, gene-editing animal models with conditional *Gzmb*-KO on NK cells are also required to further investigate the role of NK-derived GZMB in mediating hepatic IRI and liver graft injury. Furthermore, the therapeutic effect of vidarabine phosphate requires large animal LT models, discarded human liver grafts, and even prospective clinical trials in the future.

5. Conclusions

NK cells play a deleterious role by producing GZMB in graft injury in LT. Under the experimental mouse IRI or rat LT models, systemic or liver-targeted NK depletion, as well as genetic or pharmacological GZMB inhibition, could alleviate the graft injury. Targeting NK cells and derived GZMB during LT suggests potential therapeutic strategies to further improve post-transplant outcomes.

Acknowledgements

This study was funded by the National Key Research and Development Program of China (2021YFA1100500), the National Natural Science Foundation of China (82470683; U23A20513; 82200725 and 12304256), the Innovation Team of Hangzhou Medical College (CXLJ202401, China), the Key Research and Development Program of Zhejiang Province (2022C03108), Ningbo Top Medical and Health Research Program (No. 2024020818, China). The authors would like to acknowledge Shuai Wang, Nan Xu, Chang Xu, and Yiyang Sun for technical assistance. We also thank Nan Zhou and Chun Guo from the Core Facilities, Zhejiang University School of Medicine, for their technical support.

Author contributions

Xiao Xu, Xiaohui Fan, Shusen Zheng and Ruhong Zhou conceived and designed the study; Kai Wang, Zhoucheng Wang, Wenwen Ge, Yutong Chen and Zhengxing Lian performed the

experiments; Xin Shao and Chuanjun Liu performed the bioinformatic analysis; Lijun Meng performed the molecular docking and dynamics simulations; Nasha Qiu guided the construction of nanoparticles; Xiaodong Wang and Kai Wang collected the clinical samples; Kai Wang, Zhoucheng Wang, Xin Shao, Xiao Tang, Xiaohui Fan and Xiao Xu prepared the manuscript. All authors read and approved the submitted manuscript for publication.

Conflicts of interest

The authors declare no conflicts of interest.

Appendix A. Supporting information

Supporting information to this article can be found online at https://doi.org/10.1016/j.apsb.2025.07.042.

References

1. Ma Y, Wang CS, Xu GP, Yu XD, Fang ZY, Wang JL, et al. Transcriptional changes in orthotopic liver transplantation and ischemia/reperfusion injury. *Transpl Immunol* 2022;**74**:101638.
2. Jia KX, Zhang YH, Li FH, Liu RP, Wu JZ, Qu JR, et al. Acteoside ameliorates hepatocyte ferroptosis and hepatic ischemia-reperfusion injury *via* targeting PCBP2. *Acta Pharm Sin B* 2025;**15**:2077−94.
3. Liu Y, Li SP, Zhang GL, Cai JZ. NOD1 induces pyroptotic cell death to aggravate liver ischemia-reperfusion injury in mice. *MedComm* 2022;**3**:e170. 2020.
4. Jin LM, Liu YX, Cheng J, Zhou L, Xie HY, Feng XW, et al. The effect of SphK1/S1P signaling pathway on hepatic sinus microcirculation in rats with hepatic ischemia-reperfusion injury. *Hepatobiliary Pancreat Dis Int* 2022;**21**:94−8.
5. Shao X, Wang Z, Wang K, Lu XY, Zhang P, Guo RF, et al. A single-cell landscape of human liver transplantation reveals a pathogenic immune niche associated with early allograft dysfunction. *Engineering* 2024;**36**:193−208.
6. Wang ZC, Martin J, Yu JJ, Wang K, Saeb-Parsy K, Xu X. Machine perfusion plus for extended criteria donor liver grafts: making every liver count. *Engineering* 2024;**32**:29−40.
7. Li S, He J, Xu H, Yang J, Luo Y, Song W, et al. Autophagic activation of IRF-1 aggravates hepatic ischemia−reperfusion injury *via* JNK signaling. *MedComm* 2021;**2**:91−100. 2020.
8. Yamagiwa S, Kamimura H, Ichida T. Natural killer cell receptors and their ligands in liver diseases. *Med Mol Morphol* 2009;**42**:1−8.
9. Alshamary HS, Mayah QSA, Abdul-Ridha FA. The role of granzyme B activity and concentration, and serpin B9 concentration with hepatocellular carcinoma in patients with chronic hepatitis B virus. *Pakistan J Med Health Sci* 2022;**16**:464−8.
10. Guo FF, Zhang Y, Bai L, Cui JW. Natural killer cell therapy targeting cancer stem cells: old wine in a new bottle. *Cancer Lett* 2023;**570**:216328.
11. Huang M, Cai H, Han B, Xia YH, Kong XN, Gu JY. Natural killer cells in hepatic ischemia−reperfusion injury. *Front Immunol* 2022;**13**: 870038.
12. Beldi G, Banz Y, Kroemer A, Sun X, Wu Y, Graubardt N, et al. Deletion of CD39 on natural killer cells attenuates hepatic ischemia/reperfusion injury in mice. *Hepatology* 2010;**51**:1702−11.
13. Kuboki S, Sakai N, Tschöp J, Edwards MJ, Lentsch AB, Caldwell CC. Distinct contributions of $CD4^+$ T cell subsets in hepatic ischemia/reperfusion injury. *Am J Physiol Gastrointest Liver Physiol* 2009;**296**: G1054−9.
14. Valero-Pacheco N, Beaulieu AM. Transcriptional regulation of mouse tissue-resident natural killer cell development. *Front Immunol* 2020; **11**:309.
15. Chowdhury D, Lieberman J. Death by a thousand cuts: granzyme pathways of programmed cell death. *Annu Rev Immunol* 2008;**26**: 389−420.
16. Mracsko E, Liesz A, Stojanovic A, Lou WP-K, Osswald M, Zhou W, et al. Antigen dependently activated cluster of differentiation 8-positive T cells cause perforin-mediated neurotoxicity in experimental stroke. *J Neurosci* 2014;**34**:16784−95.
17. Santos-Zas I, Lemarié J, Zlatanova I, Cachanado M, Seghezzi JC, Benamer H, et al. Cytotoxic $CD8^+$ T cells promote granzyme B-dependent adverse post-ischemic cardiac remodeling. *Nat Commun* 2021;**12**:1483.
18. Shen KZ, Zheng SS, Park O, Wang H, Sun ZL, Gao B. Activation of innate immunity (NK/IFN-gamma) in rat allogeneic liver transplantation: contribution to liver injury and suppression of hepatocyte proliferation. *Am J Physiol Gastrointest Liver Physiol* 2008;**294**: G1070−7.
19. Calabrese DR, Aminian E, Mallavia B, Liu FC, Cleary SJ, Aguilar OA, et al. Natural killer cells activated through NKG2D mediate lung ischemia−reperfusion injury. *J Clin Investig* 2021;**131**: e137047.
20. Qiu NS, Liu XR, Zhong Y, Zhou ZX, Piao Y, Miao L, et al. Esterase-activated charge-reversal polymer for fibroblast-exempt cancer gene therapy. *Adv Mater* 2016;**28**:10613−22.
21. Xu SJ, Ling SB, Shan QN, Ye QW, Zhan QF, Jiang GJ, et al. Self-activated cascade-responsive sorafenib and USP22 shRNA co-delivery system for synergetic hepatocellular carcinoma therapy. *Adv Sci (Weinh)* 2021;**8**:2003042.
22. Jumper J, Evans R, Pritzel A, Green T, Figurnov M, Ronneberger O, et al. Highly accurate protein structure prediction with AlphaFold. *Nature* 2021;**596**:583−9.
23. Trott O, Olson AJ. AutoDock Vina: improving the speed and accuracy of docking with a new scoring function, efficient optimization, and multithreading. *J Comput Chem* 2010;**31**:455−61.
24. Hess B, Kutzner C, van der Spoel D, Lindahl E. G 4: algorithms for highly efficient, load-balanced, and scalable molecular simulation. *J Chem Theor Comput* 2008;**4**:435−47.
25. Humphrey W, Dalke A, Schulten K. VMD: visual molecular dynamics. *J Mol Graph* 1996;**14**(33-8):27−8.
26. Huang J, Rauscher S, Nawrocki G, Ran T, Feig M, de Groot BL, et al. CHARMM36m: an improved force field for folded and intrinsically disordered proteins. *Nat Methods* 2017;**14**:71−3.
27. Vanommeslaeghe K, Hatcher E, Acharya C, Kundu S, Zhong S, Shim J, et al. CHARMM general force field: a force field for drug-like molecules compatible with the CHARMM all-atom additive biological force fields. *J Comput Chem* 2010;**31**:671−90.
28. Kadono K, Kageyama S, Nakamura K, Hirao H, Ito T, Kojima H, et al. Myeloid Ikaros−SIRT1 signaling axis regulates hepatic inflammation and pyroptosis in ischemia-stressed mouse and human liver. *J Hepatol* 2022;**76**:896−909.
29. Wang MY, Sun JF, Yu TX, Wang MX, Jin LM, Liang SQ, et al. Diacerein protects liver against APAP-induced injury *via* targeting JNK and inhibiting JNK-mediated oxidative stress and apoptosis. *Biomed Pharmacother* 2022;**149**:112917.
30. Kimura S, Ozaki KS, Ueki S, Zhang M, Yokota S, Stolz DB, et al. Contribution of alloantigens to hepatic ischemia/reperfusion injury: roles of natural killer cells and innate immune recognition of nonself. *Liver Transplant* 2016;**22**:80−90.
31. Bi JC, Cui LL, Yu G, Yang XL, Chen YH, Wan XC. NK cells alleviate lung inflammation by negatively regulating group 2 innate lymphoid cells. *J Immunol* 2017;**198**:3336−44.
32. Vivier E, Tomasello E, Baratin M, Walzer T, Ugolini S. Functions of natural killer cells. *Nat Immunol* 2008;**9**:503−10.
33. Ikram S, Ahmad J, Durdagi S. Screening of FDA approved drugs for finding potential inhibitors against Granzyme B as a potent drug-repurposing target. *J Mol Graph Model* 2020;**95**:107462.
34. Kaiserman D, Bird CH, Sun J, Matthews A, Ung K, Whisstock JC, et al. The major human and mouse granzymes are structurally and functionally divergent. *J Cell Biol* 2006;**175**:619−30.
35. Robescu MS, Serra I, Terreni M, Ubiali D, Bavaro T. A multi-enzymatic cascade reaction for the synthesis of vidarabine 5′-monophosphate. *Catalysts* 2020;**10**:60.

36. Yang Y, Liu RG, Qu YH, Zhao JY, Tong LG, Ye SY, et al. Ghrelin ameliorates transformation of hepatic ischemia−reperfusion injury to liver fibrosis by blocking Smad and ERK signalling pathways, and promoting anti-inflammation and anti-oxidation effects. *Transpl Immunol* 2022;**73**:101597.
37. Hirao H, Nakamura K, Kupiec-Weglinski JW. Liver ischaemia-reperfusion injury: a new understanding of the role of innate immunity. *Nat Rev Gastroenterol Hepatol* 2022;**19**:239−56.
38. Wang JC, Shi Q, Zhou Q, Zhang LL, Qiu YP, Lou DY, et al. Sapidolide A alleviates acetaminophen-induced acute liver injury by inhibiting NLRP3 inflammasome activation in macrophages. *Acta Pharmacol Sin* 2022;**43**:2016−25.
39. Arias-Diaz J, Ildefonso JA, Muñoz JJ, Zapata A, Jiménez E. Both tacrolimus and sirolimus decrease Th1/Th2 ratio, and increase regulatory T lymphocytes in the liver after ischemia/reperfusion. *Lab Invest* 2009;**89**:433−45.
40. Stout-Delgado HW, Getachew Y, Rogers TE, Miller BC, Thiele DL. The role of serpinb9/serine protease inhibitor 6 in preventing granzyme B-dependent hepatotoxicity. *Hepatology* 2007;**46**: 1530−40.
41. Feng M, Li GQ, Qian XF, Fan Y, Huang XL, Zhang F, et al. IL-17A-producing NK cells were implicated in liver injury induced by ischemia and reperfusion. *Int Immunopharmacol* 2012;**13**:135−40.
42. Wang F, Birch SE, He RJ, Tawadros P, Szaszi K, Kapus A, et al. Remote ischemic preconditioning by hindlimb occlusion prevents liver ischemic/reperfusion injury: the role of High Mobility Group-Box 1. *Ann Surg* 2010;**251**:292−9.
43. Eggenhofer E, Sabet-Rashedi M, Lantow M, Renner P, Rovira J, Koehl GE, et al. RORγt^+ IL-22-producing NKp46$^+$ cells protect from hepatic ischemia reperfusion injury in mice. *J Hepatol* 2016;**64**:128−34.
44. Thomas HE, Trapani JA, Kay TW. The role of perforin and granzymes in diabetes. *Cell Death Differ* 2010;**17**:577−85.
45. Wang Z, Yin RH, Zhang L, Li SY, Zhou ZW, Sun MJ. Sulfafurazole dimers potentiate chemo-immunotherapy of low immunogenic breast cancer by preventing the PD-L1 exosomes secretion. *Acta Pharm Sin B* 2025;**15**:2673−86.
46. Kwok C, Pavlosky A, Lian DM, Jiang JF, Huang XY, Yin ZQ, et al. Necroptosis is involved in CD4$^+$ T cell-mediated microvascular endothelial cell death and chronic cardiac allograft rejection. *Transplantation* 2017;**101**:2026−37.
47. Lau A, Khan K, Pavlosky A, Yin ZQ, Huang XY, Haig A, et al. Serine protease inhibitor-6 inhibits granzyme B-mediated injury of renal tubular cells and promotes renal allograft survival. *Transplantation* 2014;**98**:402−10.
48. Lu D, Yang XY, Pan LH, Lian ZX, Tan WY, Zhuo JY, et al. Dynamic immune cell profiling identified natural killer cell shift as the key event in early allograft dysfunction after liver transplantation. *Cell Prolif* 2024;**57**:e13568.
49. Naatz LC, Dong SY, Evavold B, Ye XY, Chen MN. Bispecific killer engager for targeted depletion of PD-1 positive lymphocytes: a new avenue for autoimmune disease treatment. *Acta Pharm Sin B* 2025;**15**: 1230−41.
50. Byrne P, McGuirk P, Todryk S, Mills KH. Depletion of NK cells results in disseminating lethal infection with *Bordetella pertussis* associated with a reduction of antigen-specific Th1 and enhancement of Th2, but not Tr1 cells. *Eur J Immunol* 2004;**34**:2579−88.
51. Small CL, McCormick S, Gill N, Kugathasan K, Santosuosso M, Donaldson N, et al. NK cells play a critical protective role in host defense against acute extracellular Staphylococcus aureus bacterial infection in the lung. *J Immunol* 2008;**180**:5558−68.